Tabriz Journal of Electrical Engineering (TJEE), vol. 54, no. 4, December 2024 Serial no. 110
DOI: 10.22034/tjee.2024.58842.4739

Using a disturbance estimator in a model predictive control for single-phase current source rectifiers

Ali Hassannia, S. Masoud Barakati*, and S. Hamed Torabi

Faculty of Electrical and Computer Engineering, University of Sistan and Baluchestan, Zahedan, Iran
E-mail addresses: Ali.hassannia70@gmail.com; smbaraka@ece.usb.ac.ir; hamed.torabi@ece.usb.ac.ir
*Corresponding author

Received: 15/10/2023, Revised: 29/12/2023, Accepted: 04/02/2024.

Abstract
In this paper, first, a model predictive control (MPC) for a single-phase current source rectifier (CSR) is developed and used in electric vehicle (EV) charger structures. Due to the uncertainties in its model caused by varying points of connection to the power grid, a disturbance estimator is necessary. In addition to the uncertainties, the CSR model's precision is diminished by the rectifier output's unmodeled dynamics. The disturbance estimator with Lagrange extrapolation yields a more precise model of the single-phase CSR for MPC. Finite control set model predictive control (FCS-MPC) is employed to minimize switching losses by providing an optimal control input, eliminating the need for a modulator due to the limited number of allowable switching modes. The proposed control method is simulated in MATLAB software and implemented on a 4-kW laboratory prototype. Simulation and experimental results confirm the validity of the proposed control method.

Keywords
Electrical vehicle, current source converter, model predictive control, lagrange extrapolation, disturbance estimator.

1. Introduction

Electric vehicles have various charging methods, including direct connection to the power source, wireless charging, and battery replacement [1]. The most straightforward and readily available method is the direct connection to the power source. Charging electric vehicle batteries can be accomplished by fast charging stations in appropriate areas or by utilizing the onboard chargers of electric vehicles connected to the power grid at different locations. Manufacturers of EVs have focused more on onboard chargers because they are always present in EVs. EV chargers are categorized into unidirectional and bidirectional chargers.

Unidirectional chargers only receive power from the grid and transfer it to the vehicle's batteries. In addition to transferring power from the grid to the vehicle's batteries, bidirectional chargers can also transfer power back to the grid or another vehicle [2]–[5].

In order to reduce size, weight, and expense, onboard EV chargers can be integrated with the vehicle's propulsion system. Integrated charger structures use components of the propulsion system to charge batteries. A notable advantage of integrated structures is their capacity to charge batteries at electric motor power levels, resulting in shorter charging times [6], [7].

These structures are categorized as either isolated or non-isolated. Non-isolated structures use the electric motor windings and traction inverter as a DC/DC converter, whereas isolated structures use the electric motor windings as a low-frequency transformer [8]. In both categories of integrated structures, the challenges of demagnetization, the movement of the vehicle during charging, and the number of changes applied to the propulsion system to create the charger are among the most critical issues addressed by researchers, resulting in the development of a variety of structures with unique advantages and capabilities [9].

The structure presented in [10] is a non-isolated structure that requires minimal modifications to the propulsion system and the least amount of equipment for charging electric vehicle batteries. It is depicted in Fig. 1, and its structure's control is discussed in this article. Through the stator windings of the permanent magnet machine, a current source rectifier is connected in series with the inverter of the propulsion system in this design.

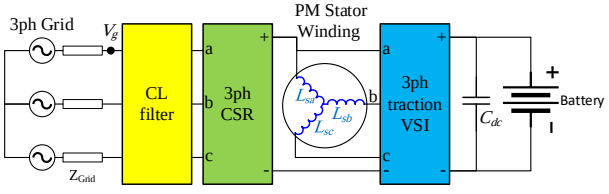

Fig. 1 The integrated charger structure with the propulsion system of electric vehicles.

A filter is required to prevent the injection of harmonic current caused by the current source rectifier switching

DOI: 10.22034/tjee.2024.58842.4739

when connecting the charger shown in Fig. 1 to the power grid. A capacitor-inductance (CL) filter usually connects current source rectifiers to the grid. Frequency resonance is a primary concern encountered in higher-order filters, and numerous solutions have been proposed in the literature to prevent or eliminate it [11], [12].

Changing the filter's parameters affects both damping and the resonance frequency, a problem that can hinder the performance of some damping techniques and, in some cases, increase resonance [13]. Changing the filter parameters in electric vehicle chargers can occur easily. Electric vehicles connect to the power grid at different points to charge their batteries, and the grid impedance changes at each connection point. The range of grid impedance changes is between 50 μH and 2 mH, as indicated in reference [14].

The grid impedance is in series with the CL filter of the CSR used in the charger structure shown in Fig. 1, so if it is changed, so will the filter specifications. In addition, these changes can reduce the controller's performance and, in some cases, lead to its instability. Thus, the uncertainty of parameters in EV chargers, resulting from a change in the connection point to the grid, poses a significant challenge for EV manufacturers. The issue of parameter uncertainty impacts the cost of EV energy consumption, the depreciation of charging system components and equipment, and the battery charging speed.

In addition, there are some standards for connecting the EV to the power grid at the residential voltage level; the onboard charger must adhere to these limitations. As the load of electric vehicles on the power grid increases, the amount of current harmonics resulting from switching increases significantly, and as a result, the power loss rises, leading to grid instability. IEC 61000-3-2 is one of the standards for connecting electrical loads whose current is less than 16 amps to the power grid at the residential voltage level. The limits of the harmonic current of the electric charge up to the fortieth order are specified separately for each harmonic in this standard, and the onboard charger must also comply.

Current source converters have higher switching losses than voltage source converters due to the more significant number of semiconductor elements, and one way to reduce switching losses in these converters is to reduce the switching frequency. Therefore, selecting a control method that generates a control input for optimal performance with a low switching frequency is essential. Finite control set model predictive control (FCS-MPC) is desirable for the three-phase current source rectifier control. This method achieves the control input with the fewest switching operations and the least defined error. Also, its switching modes are limited (9 modes), and it doesn’t need considerable calculations to generate the optimal control input.

Connecting the charger shown in Fig. 1 to a single-phase grid, where charging is more accessible than a three-phase grid, reduces the number of switching modes for FCS-MPC from nine to three and, consequently, lessens the calculation burden. However, implementing FCS-MPC is also straightforward. It does not require a modulator, one of this control method's most attractive features and benefits [15].

MPC is highly dependent on the system model, which limits its application to white box systems; however, if one provides an accurate system model, it can also be used to control uncertain systems. Using observers to increase the accuracy of the system model and enhance MPC performance is one of the solutions for providing an accurate system model. With this knowledge, in the structure of Fig. 1, parametric uncertainty manifests as a mismatched disturbance in CSR state equations [13]. In most control systems, estimation-based methods are used to reduce the impact of mismatched disturbances [16]. The control input incorporates disturbance estimation in these methods. Consequently, this is an additional reason to use the disturbance estimator to regulate the CSR of Fig. 1.

The cost function definition that describes the control objective is the most essential part of MPC design. The cost function is defined in [17], [18] to regulate the output current's ripple and instantaneous reactive power in a three-phase CSR. In addition to controlling the ripple of the output current in [19], the cost function is designed to mitigate frequency resonance by modelling the virtual resistance in parallel with the filter capacitor. The cost function also can be altered concerning other control objectives to minimize switching frequency. Hence, in [20], the control objectives include active and reactive power control, eliminating the effect of grid harmonics on the converter and reducing the switching frequency.

It is also possible to eliminate frequency resonance by tracking the inductor current and capacitor voltage simultaneously. In simpler terms, the simultaneous tracking of these two variables is the implementation of the active damper in the cost function, which controls the resonance frequency and damping [21]. In [22], in addition to the mentioned objectives, the effect of parameter changes has also been investigated, and the cost function can neutralize its effects on the converter's performance. Two separate observers estimate the capacitor voltage reference and the inductor current reference.

In the cited references dealing with the control of the three-phase CSR, the objective is to control the current on the DC side, but for Fig. 1's CSR, the objective is to control the current on the AC side and power factor. Furthermore, CSR dynamics are easily obtained but not in the charger structure, and considering output dynamics only increases control complexity. In the structure depicted in Fig. 1, the inverter switch legs feeding the permanent magnet electric motor serve as an interleaved boost, which regulates the ripple of the output current. Separate from the rectifier control, a hysteresis or proportional-integral (PI) controller can control the interleaved boost converter.

In this paper, FCS-MPC is designed for the CSR shown in Fig. 1, which is powered by a single-phase grid. The control objectives are to control the power factor at the converter's input, control the current's harmonic content on the grid side, and comply with the IEC 61000-3-2 limits despite changes in grid impedance. The Lagrange extrapolation estimates the mismatched disturbance caused by parameter uncertainties. Moreover, the dynamics on the DC side are considered as a cumulative

DOI: 10.22034/tjee.2024.58842.4739

disturbance in the state equations, which are also estimated by the Lagrange extrapolation method.

In general, a robust and simple control in terms of calculations and complexity is proposed so that it can be easily applied to electric vehicles. The contribution of this article are summarized as follows:

- Compensation for calculation delays in MPC in the presence of disturbances in system state equations.
- Estimating parametric uncertainty by converting it into an additive term and through data from previous steps.
- CSR control to adjust the AC side current independently of the DC side, which reduces control complexity.
- Optimized and robust charger control due to MPC and disturbance estimator, respectively.

In the second section of this paper, the charger's rectifier is modelled, and in the third section, the MPC is designed for it. The fourth section discusses simulation results and the practical application of the proposed method on a laboratory prototype. The article's conclusion is presented in the fifth section.

2. Current Source Rectifier Modelling

The circuit in Fig. 1's charger structure is simplified in Fig. 2, assuming a constant output for the CSR and feeding it through a single-phase grid. In Fig. 2, the grid is connected to the first and second phases of the three-phase rectifier. For the sake of simplicity, the values of the inductor and the filter capacitor, which are in series, have been converted so that they can be modeled using the same symbols as in Fig. 1.

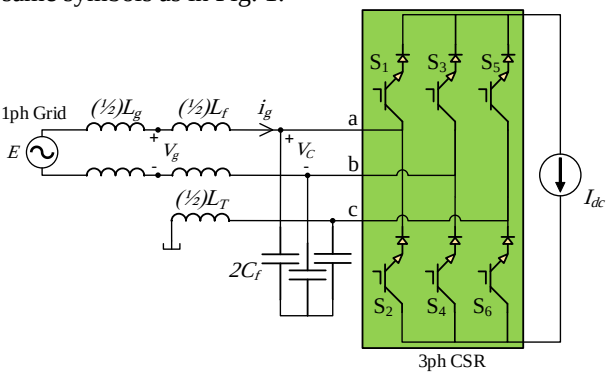

Fig. 2 A three-phase CSR connected to a single-phase grid

Equation (1) is obtained by applying Kirchhoff's voltage law (KVL) and Kirchhoff's current law (KCL) to the circuit depicted in Fig. 2.

$$\begin{cases} -E + (L_f + L_g)\dot{i_g} + r_t i_g + V_c = 0 & (a) \\ i_g = C_f \dot{V_c} + I_{dc} u & (b) \end{cases} \quad (1)$$

where E is the grid voltage, L_f filter inductance, L_g grid inductance, i_g grid current, V_c capacitor voltage, r_t is the equivalent resistance of the filter inductance and grid inductance, C_f is the filter capacitor, I_{dc} is the output current of the rectifier, and u is the switching function or control input. The L_g parameter appears as a multiplier in the state variable when the capacitor voltage and grid current are considered system state variables. The grid inductance effect, representing the system's uncertainty, should be included as a cumulative term in the state equations to simplify the controller design procedure. Therefore, equation (1)(a) must be modified. For this purpose, the voltage of the charger's connection point to the grid is substituted for the grid voltage in the KVL equation, and the state equations are rewritten as (2).

$$\begin{cases} \dot{i_g} = -\frac{r_t}{L_f} i_g - \frac{1}{L_f} V_c + \frac{1}{L_f} V_g \\ \dot{V_c} = \frac{1}{C_f} i_g - \frac{1}{C_f} I_{dc} u + d_2 \end{cases} \quad (2)$$

where V_g represents the voltage at the charger's connection point to the grid and is represented in the equations as a cumulative term. d_2 is the previously overlooked DC-side dynamic effect. Therefore, in (2), L_T, which contained uncertainty, was replaced with L_f so that uncertainty appears as an additive term (V_g) in the state equations. Converting the state equations into standard form (3) before designing the controller and disturbance estimator is preferable. It is necessary to estimate the vector $d = [d_1, d_2]^T$, which represents the cumulative disturbances of the system (3), to improve its precision.

$$\begin{cases} \dot{x} = Ax + Bu + d \\ y = Cx \end{cases} \quad (3)$$

$$x = \begin{bmatrix} i_g \\ V_c \end{bmatrix}, A = \begin{bmatrix} -\frac{r_t}{L_f} & -\frac{1}{L_f} \\ \frac{1}{C_f} & 0 \end{bmatrix}$$

$$, B = \begin{bmatrix} 0 \\ -\frac{1}{C_f} I_{dc} \end{bmatrix}, C = \begin{bmatrix} 1 & 0 \\ 0 & 1 \end{bmatrix}$$

$$, d = \begin{bmatrix} \frac{1}{L_f} V_g \\ d_2 \end{bmatrix}$$

where A is the state matrix, B is the input coefficients matrix, C is the output coefficients matrix, x is the state variables vector, d is the disturbance vector, and y is the output vector. After converting the state equations to the standard form (3), they must be converted to discrete-time form because they are used for design and implementation. The zero-order hold (ZOH) method discretizes the state equations, and various methods can approximate it; Euler's method is used more due to its simplicity. This method, however, needs to improve in approximation. The switching frequency can be increased to improve accuracy. On the other hand, reducing the switching frequency in current source converters reduces losses and, as a result, the sampling frequency, which affects the accuracy of the Euler approximation. Increasing the number of terms in the Euler approximation could be a solution. It is worth noting that methods with high accuracy can be used for discretization. However, this increases the system's complexity and the computational burden for implementation [23]. The discrete-time format of (3) is presented in (4).

$$X_{k+1} = \mathrm{A}_d X_k + \mathrm{B}_d U_k + d_k \quad (4)$$

DOI: 10.22034/tjee.2024.58842.4739

$$X_k = x(kT_s), U_k = U(kT_s),$$
$$d_k = d(kT_s),\ A_d = e^{AT_s},$$
$$B_d = \int_0^{T_s} e^{A\tau} d\tau B,$$
$$d_k = \int_0^{T_s} e^{A\tau} d\big((k+1)T_s - \tau\big) d\tau$$

where T_s is the sampling time and k is the sampling step. The first three terms of Euler's approximation are used to approximate the coefficients of the system (4). Estimating the value of d_k is essential for MPC design. In an earlier step, disturbances can be approximated as an additive term using equation (4). According to (5), the disturbance vector value in a previous step is calculated with the measured values of the state variables at the present and a previous step. However, for equation (4), estimating the disturbance value at the present step is necessary, which can be achieved using the Lagrange extrapolation method [24].

$$d_{k-1} = X_k - \mathrm{A}_d X_{k-1} - \mathrm{B}_d U_{k-1} \quad (5)$$

In the Lagrange extrapolation method, the amount of disturbance can be estimated using the data from the previous steps, whose relation is given in (6).

$$\hat{d}_k = \sum_{i=0}^{n} (-1)^{n-i} \begin{bmatrix} n+1 \\ i \end{bmatrix} d_{k+i-n-1} \quad (6)$$

where n is the number of previous steps for estimation. In the Lagrange method, as given in (6), the disturbance value is calculated by the algebraic sum of the data stored in the previous steps, and the coefficient of each term is calculated according to its proximity to the desired step. Therefore, $\hat{d}_k$ is substituted for $\mathrm{d_k}$ in (4) for MPC design, and system (4) becomes (7).

$$\hat{X}_{k+1} = \mathrm{A}_d X_k + \mathrm{B}_d U_k + \hat{d}_k \quad (7)$$

3. Model Predictive Control Designing

The most critical aspect of MPC design is defining the cost function, which also defines the control objective. The primary purpose of controlling the CSR charger (Fig. 1) is to control the grid side current. As a result, there must be a statement in the cost function that traces the grid current reference. Capacitor voltage tracking must also be incorporated into the cost function to increase the power factor, decrease distortion, and minimize harmonic power losses. The operation of a virtual impedance is similar to that of an actual impedance, except that it lacks the real impedance losses. Considering a resistor in parallel with a capacitor, for instance, this resistor is a path for passing harmonic currents, but since it does not exist, it does not consume power. To realize this virtual resistance in parallel with the capacitor, a term in the cost function that represents the harmonic current error that passes through the virtual impedance can be considered. Consequently, the cost function consists of three terms: grid current tracking, capacitor voltage tracking, and harmonic current error.

In defining the cost function in FCS-MPC by predicting the system's behaviour in the next step, the value of the control input is determined so that the cost function has the lowest value. Due to the real-time nature of the calculation of the control input, the delay in applying the input to the system is caused by the calculations. The delay in applying the control input increases the system output ripples, and the tracking is incorrect. Therefore, the delay in applying the input should be eliminated somehow. Predicting the system's behaviour in the next two steps and then calculating the control input for the next step is a common technique for eliminating the delay. Thus, at the start of each sampling step, the control input calculated in the previous step is first applied, followed by the calculation of the control input for the subsequent step. The cost function in (8) is defined for the next two steps, predicting the next step's control input.

$$J = \alpha(i^*_{g,k+2} - \hat{X}_{1,k+2})^2 + \beta(V^*_{c,k+2} - \hat{X}_{2,k+2})^2 + \gamma(i^p_{gh,k+2} - i^p_{gv,k+2})^2 \quad (8)$$

where α, β, and γ are constant coefficients, $i^*_{g,k+2}$ and $V^*_{c,k+2}$ are respectively the grid current and capacitor voltage references for the next two steps, $\hat{X}_{1,k+2}$ and $\hat{X}_{2,k+2}$ are respectively the predicted values of the first and second state variables for the next two steps, $i^p_{gh,k+2}$is the predicted grid harmonic current for the next two steps and $i^p_{gv,k+2}$ is the predicted harmonic current passing through the virtual resistance for the next two steps. In the following two steps, (9) can be utilized to derive the system state equations. In (9), $\hat{X}_{k+1}$ is derived from (7), and to determine the value of $\hat{d}_{k+1}$, the Lagrange extrapolation method should be applied, with the exception that k+1 should be substituted for k in (6). Determining the value of the disturbance in step k+1 requires estimating the disturbance in step k, which is estimated in (6).

$$\hat{X}_{k+2} = \mathrm{A}_d \hat{X}_{k+1} + \mathrm{B}_d U_{k+1} + \hat{d}_{k+1} \quad (9)$$

In relation (9), the state variables are predicted in the next two steps, and to track these state variables that are given in the objective function (8), reference values for the variables must be defined in the next two steps. The reference value of the grid current is a sine wave in phase with the capacitor voltage, whose amplitude is proportional to the amplitude of the rectifier's output current and the modulation index selected [13]. The sine-wave argument is obtained using a phase-locked loop (PLL) based on the capacitor voltage, and its amplitude is a proportion of the DC/DC converter's required input current reference. Equation (10) yields the current reference value via vector representation.

$$i^*_{g,k} = |I_{gs} \mathrm{e}^{j\theta(k)}| \quad (10)$$
$$I_{gs} = mI^*_{DC}$$
$$\theta(k) = 2\pi f_i k T_s + \theta_0$$

where the function *θ(k)* is the PLL output, m modulation index, and f_i is the grid frequency. Equation (11) provides the current reference value for the next two steps, one advantage of its vector representation.

$$i^*_{g,k+2} = |i^*_{g,k} \mathrm{e}^{j4\pi f_i T_s}| \quad (11)$$

The capacitor voltage reference is also a sine wave whose amplitude is proportional to the reference active power and is derived from equation (12).

$$V_{cs} = \frac{P^*}{I_{gs}} \quad (12)$$

DOI: 10.22034/tjee.2024.58842.4739

where V_{cs} is the voltage reference rms value and P^* is the active power reference value of the converter. Like the grid current reference, the capacitor voltage reference is defined in equation (13), and its value is obtained for the two next steps in equation (14).

$$V_{c,k}^{*} = |V_{cs} e^{j\theta(k)}| \quad (13)$$

$$V_{c,k+2}^{*} = |V_{c,k}^{*} e^{j4\pi f_i T_s}| \quad (14)$$

In the final stage of MPC design, the variables of the third term of the cost function (8) are specified. The measured current's harmonic content causes its predicted value to include harmonics in the next two steps. In the next two steps, the harmonic content $i_{gh,k+2}^{p}$ is obtained by passing the predicted current value through the high-pass filter. The predicted harmonic current must flow through the parallel virtual resistance to the capacitor, and the current's value can be calculated using equation (15).

$$i_{gv,k+2}^{p} = \frac{\hat{X}_{2h,k+2}}{R_v} \quad (15)$$

Where R_v is the virtual resistance and $\hat{X}_{2h,k+2}$ is the harmonic content of the predicted capacitor voltage in the next two steps. Similar to the grid current, the harmonic content of the predicted capacitor voltage is obtained by passing it through the high-pass filter.

Fig. 3 depicts the implementation of the designed FCS-MPC, which corresponds to the design procedure.

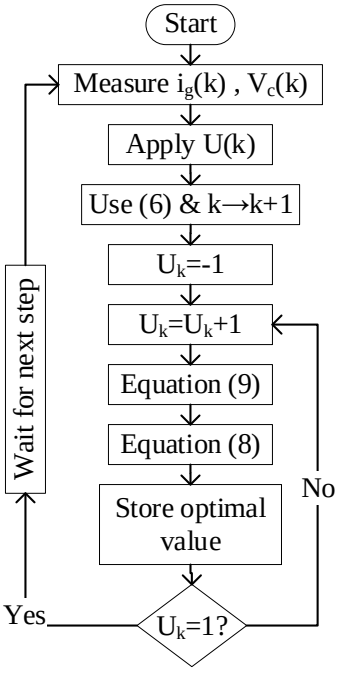

Fig. 3 MPC implementation algorithm for the CSR used in the charger structure

After designing the MPC for the current source rectifier and implementing the hysteresis controller for the interleaved boost converter, the proposed control block diagram for the charger shown in Fig. 1 is obtained as shown in Fig. 4.

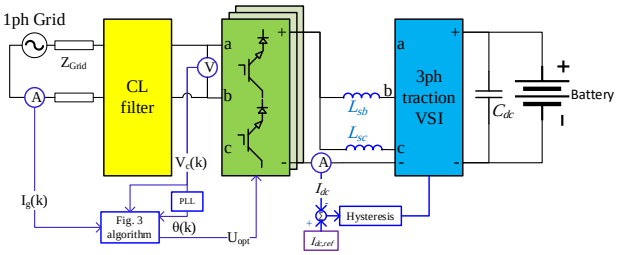

Fig. 4 EV Charger structure and its control blocks

3.1. *Parameter Design*

The control structure depicted in Fig. 4 requires several parameters for its implementation, including three parameters for MPC, virtual resistance for the filter, the reference for the output current, and the modulation index. The IEC 61000-3-2 standard applies to equipment with an input current of less than 16 amperes (rms). In order to assess the controller's performance under the most unfavorable conditions as per the standard, it is imperative to configure the output current reference and modulation index in a manner that results in the input current reference being set at 16 amperes (rms), as specified in equation (10).

Determining the magnitude of virtual resistance is a complex matter that relies on its specific definition. This paper examines the concept of virtual resistance, which is connected in parallel with the capacitor and utilizes feedback from the capacitor voltage. Thus, this resistance solely affects the damping of the CL filter. The optimal damping rate for the filter can be calculated by utilizing equation (16) to ascertain its value [21].

$$\xi = -\frac{R_v}{2}\sqrt{\frac{L_f}{C_f}} \quad (16)$$

where ξ is damping rate, and by determining this, the virtual resistance value is calculated. The three parameters, α, β, and γ, also are the coefficients of the tracking errors specified in the cost function, which have values ranging from 0 to 1. The most straightforward approach to ascertain them is through trial and error. It is essential to recognize that these coefficients modify the sensitivity of the cost function to the tracking error of the variables being considered; furthermore, the error ranges differ. Consequently, with this knowledge, it becomes explicit to ascertain the coefficients' values.

As defined in equation (6), the disturbance estimator utilizes the Lagrange extrapolation method and necessitates only a single parameter, denoted as n. This parameter depends on the sampling frequency and the type of the signal to be estimated. Determining this parameter is a trade-off between accuracy and the volume of stored data and computations [24].

4. Simulation and Experimental Results

4.1. *Simulation*

The control diagram block shown in Fig. 4 is simulated in MATLAB to confirm the proposed method's accuracy. Since battery charging modes are not the focus of this article, a resistor is used instead of the battery in the simulation and experimental implementation of the control method. Additionally, separate core inductors are used instead of the permanent magnet machine's stator windings' inherent inductance property. It should be noted

DOI: 10.22034/tjee.2024.58842.4739

that substituting the mentioned elements does not pose a problem in the simulation process or obtaining the results; it was done solely for convenience. The elements and parameters of the simulated Fig. 4 are listed in Table I.

Table I values of charger circuit parameters and elements

Parameter	Value
Filter Capacitance (C_f)	60 µF
Filter Inductance (L_f)	5 mH
Grid Inductance (L_g)	0.1-1 mH
Grid Voltage (E)	220 V (RMS)
n in Lagrange extrapolation	3
Modulation index (m)	0.86
Output current reference (I_{dc}^*)	26
α in MPC	0.9512
β in MPC	0.1
γ in MPC	0.3
ξ	0.7

The change of the grid impedance from 100 µH to 1 mH is the scenario investigated to validate the performance of the proposed control method. A series voltage source with a variable inductor is considered a single-phase grid to implement this scenario. In Fig. 5(a) and Fig. 5(b), the waveforms of capacitor voltage and grid current for two different grid inductance values are depicted, respectively. As shown in Fig. 5, the phase difference between the capacitor voltage and the grid current is negligible, indicating that the controller operates perfectly to correct the power factor. In addition, the shape of the waves is of high quality, with acceptable distortion; however, their quality must be evaluated by the indicators. Fig. 6 is associated with the IEC 61000-3-2 standard and depicts the harmonic spectrum of the grid current for two distinct grid inductance values. In this graph, the permitted value for each harmonic is represented by green columns. The value of each order of the grid current harmonic is also depicted in blue and to the left of the permissible value columns. In both cases, the standard limits have been met, and the THD is below 5%, confirming the high quality of the results. The resonance frequency and filter attenuation can be changed by changing the amount of the inductor. In some instances, it may intensify the frequency resonance of one of the switching harmonics; however, in other cases, this may not occur, and the harmonic may not be amplified. Therefore, the increase or decrease of the inductor alone is not the only factor that changes THD, and it is impossible to predict the decrease or increase of THD by changing it. Due to this, the amount of THD in both simulation modes is similar, whereas the amount of harmonics in the grid current's frequency spectrum differs.

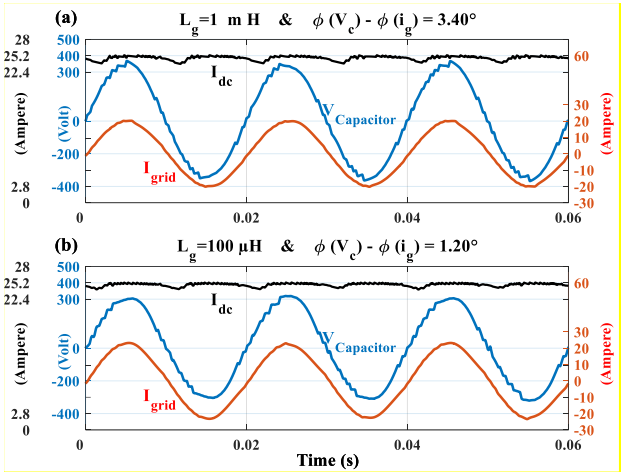

Fig. 5 simulated grid current and capacitor voltage waveforms with a) 1 mH grid inductance, b) 100 µH grid inductance

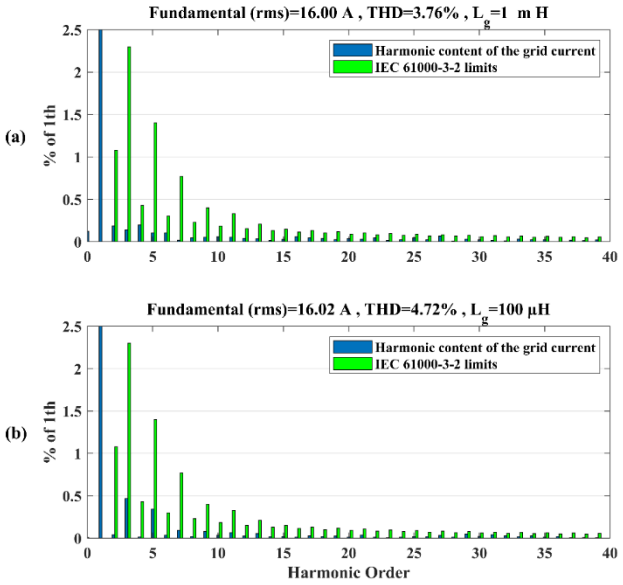

Fig. 6 Harmonic spectrum of grid current in the simulation of the proposed method with a) 1 mH grid inductance and b) 100 µH grid inductance.

4.2. Experimental Results

The proposed method has been applied to a laboratory prototype with 4 kW power, as shown in Fig. 7. The TI's TMS320F28335 DSP generates the pulses that activate the converter switches. This DSP implements separate controllers for the rectifier and DC/DC converter.

DOI: 10.22034/tjee.2024.58842.4739

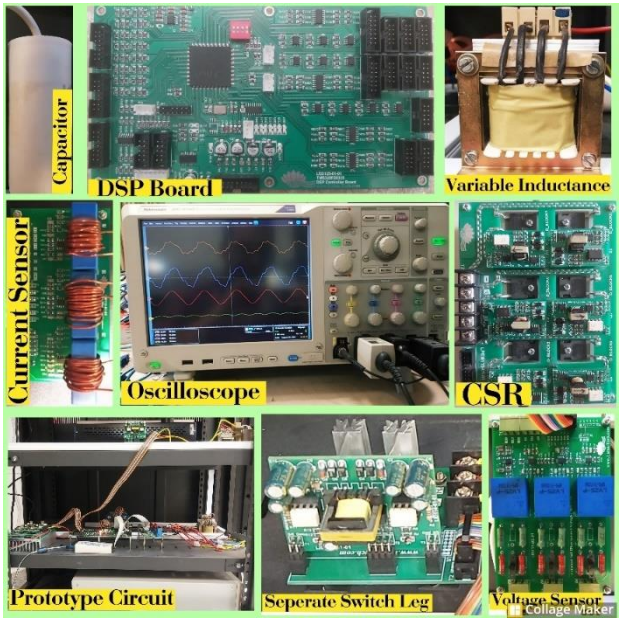

Fig. 7 Laboratory prototype's components.

The same grid impedance change scenario is also considered for the experimental implementation of the proposed method. Fig. 8 depicts the oscilloscope's output about the waveforms of the capacitor voltage and grid current with the 1 mH grid inductance. The grid current's RMS value is 15.5 amps, and its THD is 7%. The active power calculated by the oscilloscope is 3300 watts, and the PF of the converter is 97%. Therefore, both the power factor is controlled, and the quality of the results is satisfactory.

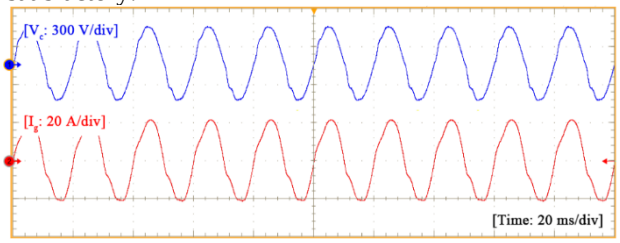

Fig. 8 Grid current and capacitor voltage waveforms with 1 mH grid inductance in the experimental implementation of the proposed method

The IEC 61000-3-2 standard is also analyzed with an oscilloscope, and Fig. 9 depicts the output in which the harmonic content is magnified. The column chart of the harmonic content of the grid current, along with the standard limits, is depicted in Fig. 9. In each order of harmonics, the thin columns represent the standard limit, while the thick columns represent the grid current harmonic value. All thick columns are shorter than thin ones in the harmonic spectrum, indicating conformity with the standard.

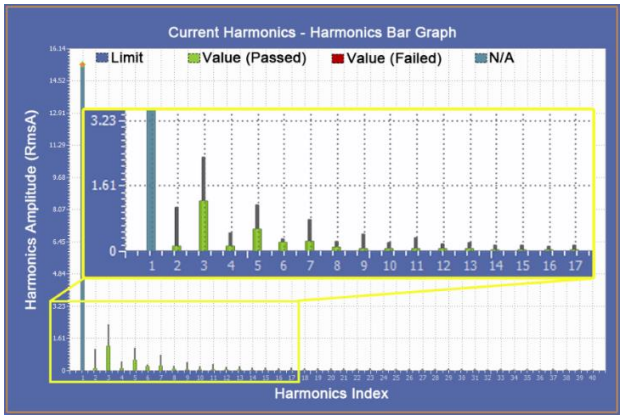

Fig. 9 Harmonic spectrum of grid current with 1 mH grid inductance in the experimental implementation of the proposed method

The experiment is repeated for a grid inductance of 100μH, and the results are depicted in Fig. 10. In this case, harmonic distortion increases for both capacitor voltage and grid current waveforms, and the current THD reaches 8.5%. The grid current has an RMS value of 16.13 amps, and the active power is 3,410 watts.

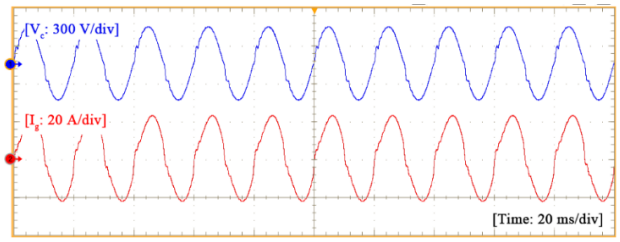

Fig. 10 Grid current and capacitor voltage waveforms with 100 μH grid inductance in the experimental implementation of the proposed method

In Fig. 11, the harmonic spectrum of the grid current is shown when the grid inductance is 100 μH. This figure demonstrates that the standard for connecting the charger to the grid is also adhered to.

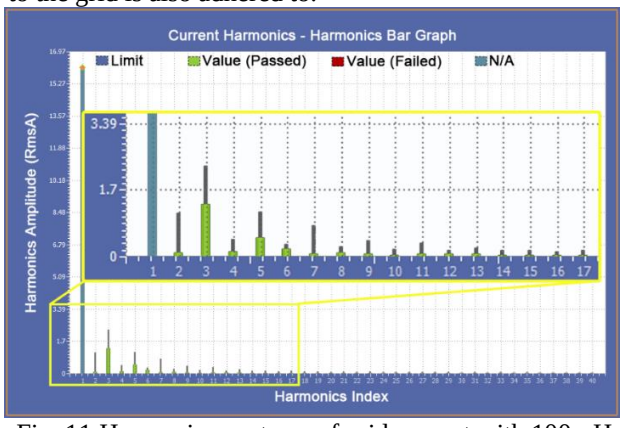

Fig. 11 Harmonic spectrum of grid current with 100 μH grid inductance in the experimental implementation of the proposed method

Two references [13] and [14] specifically worked in robust control of the current source rectifier used in the structure of EV onboard chargers. In [13], with sliding mode control and a Lagrange extrapolation-based disturbance estimator, an attempt has been made to make the controller robust against grid impedance changes. This

DOI: 10.22034/tjee.2024.58842.4739

goal has been achieved well in this reference. However, the control input is not optimal and oscillates due to the chattering phenomenon. The adaptive virtual resistance value in [14] varies based on conditions, and an attempt has been made to modify the damping ratio of the filter to suppress frequency resonance within the grid's impedance change range. Despite the simple control structure employed in this reference, the determination of the virtual resistance value is intricate, which imposes a heavy computational load on the microcontroller. The method proposed in this paper effectively addresses the problem by utilizing data from previous steps and implementing a straightforward MPC structure. Furthermore, it optimizes the control input to minimize switching losses.

5. Conclusion

An MPC based on a disturbance estimator is presented for a single-phase CSR used in an EV charger structure. The advantage of the Lagrange extrapolation-based disturbance estimator is that it presents the system model in the next two steps. One approach to remedy the delay in implementing the control input is utilizing the system model in the next two steps, which is constructed using the Lagrange technique. In addition, the proposed method is robust to changes in system parameters and unmodeled dynamics, as demonstrated by the simulation and experimental results in the presence of grid impedance changes. Power factor control and compliance with connection standards are other control objectives that the results show are correctly met. THD is less than 5% in the simulation results for both grid impedance value scenarios and slightly higher in the implementation results. The power factor correction is done correctly in both scenarios, whether in simulation or practical implementation, and is close to unity. The results in all cases are compared to the IEC 61000-3-2 standard, and all limitations are passed. Despite parameter changes and unmodeled dynamics, the proposed control method has generally achieved the desired results.

References

[1] Q. Kong and H. Zheng, “Study on Automated Alignment Methods for Electric Vehicles Wireless Charging,” in *Proceedings - 2022 International Conference on Mechanical, Automation and Electrical Engineering, CMAEE 2022*, 2022. doi: 10.1109/CMAEE58250.2022.00038.

[۲] علیرضا. حاتمی، پیمان. بیات، پژمان. بیات، و سیدمحمدرضا. طوسی، «ارائه یک استراتژی جدید برای مدیریت انرژی خودروی الکتریکی مبتنی بر مبدل دوطرفه سه‌درگاهه و کنترل‌کننده فازی»، مجله مهندسی برق دانشگاه تبریز، جلد ۴۶، شماره ۳، صفحه ۱۲۱-۱۳۷، ۱۳۹۴.

[3] J. Lara, C. Hernández, M. Arjona, L. Masisi, and A. Chandra, “Bidirectional EV charger with ancillary power quality capabilities,” *Ing. Investig. Tecnol.*, vol. 23, no. 1, pp. 1–10, Jan. 2022, doi: 10.22201/fi.25940732e.2022.23.1.008.

[4] C. A. Sam and V. Jegathesan, “Bidirectional integrated on-board chargers for electric vehicles—a review,” *Sādhanā*, vol. 46, no. 1, p. 26, Dec. 2021, doi: 10.1007/s12046-020-01556-2.

[5] G. Anjinappa, D. B. Prabhakar, and W.-C. Lai, “Bidirectional Converter for Plug-In Hybrid Electric Vehicle On-Board Battery Chargers with Hybrid Technique,” *World Electr. Veh. J.*, vol. 13, no. 11, p. 196, Oct. 2022, doi: 10.3390/wevj13110196.

[6] T. J. C. Sousa, D. Pedrosa, V. Monteiro, and J. L. Afonso, “A Review on Integrated Battery Chargers for Electric Vehicles,” *Energies*, vol. 15, no. 8, p. 2756, Apr. 2022, doi: 10.3390/en15082756.

[7] U. Mustafa, R. Ahmed, A. Watson, P. Wheeler, N. Ahmed, and P. Dahele, “A Comprehensive Review of Machine-Integrated Electric Vehicle Chargers,” *Energies*, vol. 16, no. 1, p. 129, Dec. 2022, doi: 10.3390/en16010129.

[8] N. Sakr, D. Sadarnac, and A. Gascher, “A review of on-board integrated chargers for electric vehicles,” in *2014 16th European Conference on Power Electronics and Applications*, IEEE, Aug. 2014, pp. 1–10. doi: 10.1109/EPE.2014.6910865.

[9] S. Jaman, S. Chakraborty, D.-D. Tran, T. Geury, M. El Baghdadi, and O. Hegazy, “Review on Integrated On-Board Charger-Traction Systems: V2G Topologies, Control Approaches, Standards and Power Density State-of-the-Art for Electric Vehicle,” *Energies*, vol. 15, no. 15, p. 5376, Jul. 2022, doi: 10.3390/en15155376.

[10] C. Shi, Y. Tang, and A. Khaligh, “A Three-Phase Integrated Onboard Charger for Plug-In Electric Vehicles,” *IEEE Trans. Power Electron.*, vol. 33, no. 6, pp. 4716–4725, Jun. 2018, doi: 10.1109/TPEL.2017.2727398.

[11] X. Ruan, X. Wang, D. Pan, D. Yang, W. Li, and C. Bao, *Control Techniques for LCL-Type Grid-Connected Inverters*. in CPSS Power Electronics Series. Singapore: Springer Singapore, 2018. doi: 10.1007/978-981-10-4277-5.

[12] J. Xu and S. Xie, “LCL-resonance damping strategies for grid-connected inverters with LCL filters : a comprehensive review,” *J. Mod. Power Syst. Clean Energy*, vol. 6, no. 2, pp. 292–305, 2018, doi: 10.1007/s40565-017-0319-7.

[13] A. Hassannia, S. M. Barakati, and S. H. Torabi, “Robust discrete sliding mode controller design for a single-phase onboard integrated electric vehicle charger with disturbance estimation,” *Comput. Electr. Eng.*, vol. 110, p. 108881, Sep. 2023, doi: 10.1016/j.compeleceng.2023.108881.

[14] C. Saber, D. Labrousse, B. Revol, and A. Gascher, “Challenges Facing PFC of a Single-Phase On-Board Charger for Electric Vehicles Based on a Current Source Active Rectifier Input Stage,” *IEEE Trans. Power Electron.*, vol. 31, no. 9, pp. 6192–6202, Sep. 2016, doi: 10.1109/TPEL.2015.2500958.

[۱۵] پیمان. حق گویی، داود. عرب خابوری، مهیار. خسروی، «ارائه روشی ترکیبی مبتنی بر رویکرد کنترلی پیش‌بین مدل به‌منظور کنترل طبقه یکسوساز ترانسفورماتور الکترونیک قدرت»، مجله مهندسی برق دانشگاه تبریز، جلد۴۹، شماره ۳، صفحه ۱۰۶۷-۱۰۷۹، ۱۳۹۸.

[16] W.-H. Chen, S. Li, and J. Yang, “Non-linear disturbance observer-based robust control for systems with mismatched disturbances/uncertainties,” *IET*

DOI: 10.22034/tjee.2024.58842.4739

Control Theory Appl., vol. 5, no. 18, pp. 2053–2062, Dec. 2011, doi: 10.1049/iet-cta.2010.0616.
[17] P. Correa, J. Rodriguez, I. Lizama, and D. Andler, "A Predictive Control Scheme for Current-Source Rectifiers," *IEEE Trans. Ind. Electron.*, vol. 56, no. 5, pp. 1813–1815, May 2009, doi: 10.1109/TIE.2008.2010116.
[18] P. Correa and J. Rodriguez, "A predictive control scheme for current source rectifiers," in *2008 13th International Power Electronics and Motion Control Conference*, IEEE, Sep. 2008, pp. 699–702. doi: 10.1109/EPEPEMC.2008.4635346.
[19] H. Gao, B. Wu, D. Xu, M. Pande, and R. P. Aguilera, "Model predictive control scheme with active damping function for current source rectifiers," *IET Power Electron.*, vol. 10, no. 7, pp. 717–725, Jun. 2017, doi: 10.1049/iet-pel.2016.0718.
[20] C. Xue, L. Ding, Y. Li, and N. R. Zargari, "Improved Model Predictive Control for High-Power Current-Source Rectifiers under Normal and Distorted Grid Conditions," *IEEE Trans. Power Electron.*, vol. 35, no. 5, pp. 4588–4601, 2020, doi: 10.1109/TPEL.2019.2946251.
[21] Z. Bai, H. Ma, D. Xu, B. Wu, Y. Fang, and Y. Yao, "Resonance Damping and Harmonic Suppression for Grid-Connected Current-Source Converter," *IEEE Trans. Ind. Electron.*, vol. 61, no. 7, pp. 3146–3154, Jul. 2014, doi: 10.1109/TIE.2013.2281173.
[22] C. Xue, L. Ding, X. Wu, Y. Li, and W. Song, "Model Predictive Control for Grid-Connected Current-Source Converter With Enhanced Robustness and Grid-Current Feedback Only," *IEEE J. Emerg. Sel. Top. Power Electron.*, vol. 10, no. 5, pp. 5591–5603, Oct. 2022, doi: 10.1109/JESTPE.2022.3162140.
[23] H. M. Shertukde, Digital Control Applications Illustrated with MATLAB. 2015.
[24] F. B. Hildebrand, *Introduction to Numerical Analysis*. McGraw-Hill, 1956.